Mechanisms and Active Control of Jet-Induced Noise

Andreas Babucke, Bruno Spagnoli, Christophe Airiau, Markus Kloker, and Ulrich Rist

Abstract Fundamental mechanisms of jet noise are investigated by means of direct numerical simulation. In the mixing layer, subharmonics of the respective vortex pairing are found to be responsible for the main part of the generated noise which is directed in downstream direction. By modifying the phase shift between introduced disturbances it is possible to diminish or enhance relevant portions of the emitted sound. Optimal control has been applied successfully to a plane mixing layer. In the far field, the mean noise level could be reduced. Depending on the measurement line, some distributed control or anti-noise is generated by the control. A more realistic configuration is achieved by adding a splitter plate representing the nozzle end. Rectangular serrations lead to a breakdown of the large coherent spanwise vortical structures and thus provide a noise reduction of 9dB.

1 Introduction

Noise reduction is of great interest for a variety of technical applications. This is especially the case in aviation. Since most airports are located in highly populated areas, the reduction of aircraft noise can improve the quality of life for many people. Especially during take-off, jet noise is the largest aeroacoustic source of an aircraft. Recent reductions of jet noise are mainly due to an increased bypass ratio in the turbojet engine. Currently a geometric variation of the nozzle end is considered, known as chevron-nozzle. Its noise reduction is often explained by an increased

Andreas Babucke · Markus J. Kloker · Ulrich Rist
Institut für Aerodynamik und Gasdynamik (IAG), Universität Stuttgart, Pfaffenwaldring 21 D-70550 Stuttgart, e-mail: babucke@iag.uni-stuttgart.de

Bruno Spagnoli · Christophe Airiau
Université de Toulouse, Paul Sabatier, Institut de Mécanique des Fluides de Toulouse (IMFT), Allée du professeur Camille Soula, F-31400 Toulouse e-mail: airiau@imft.fr

mixing behind the trailing edge of the nozzle. However the underlying physical mechanisms are not yet fully understood.

Within the subproject 5 *Mechanisms and Active Control of Jet-induced Noise*, the mechanisms of noise generation and its reduction are investigated using direct numerical simulations (DNS). Such aeroacoustic simulations face several difficulties due to largely different scales of flow field and acoustics. The hydrodynamic fluctuations are small-scale structures containing high energy compared to the acoustics with relatively large wavelengths and small amplitudes. Therefore, high resolution is required to compute the noise sources accurately. On the other hand a large computational domain is necessary to obtain the relevant portions of the acoustic far-field. Due to the small amplitudes of the emitted noise, boundary conditions have to be chosen carefully, in order not to spoil the acoustic field with reflections.

Since computational resources are limited, one possibility is the simulation of low-Reynolds-number jets, e.g. done by Freund [12]. Our focus is set on the mixing layer behind the nozzle end which is responsible for the most anoying high-frequency noise. As sketched in figure 1, mixing layers occur between the primary and the bypass stream and between the bypass stream and the freestream. Having high Reynolds-number jets at an aircraft's engine, the large diameter allows to neglect curvature. This approach is widely used [6, 9] for large-eddy or direct numerical simulations, where an S-shaped velocity profile is prescribed at the inflow. This flow field allows to investigate the fundamental mechanisms of noise generation and its control. Beyond this, the nozzle end can be included in the simulation, leading to a combination of wake and mixing layer. This provides a more realistic configuration and allows to simulate wall-mounted actuators. In this context, the engrailed nozzle end can be interpreted as a first passive 'actuator'.

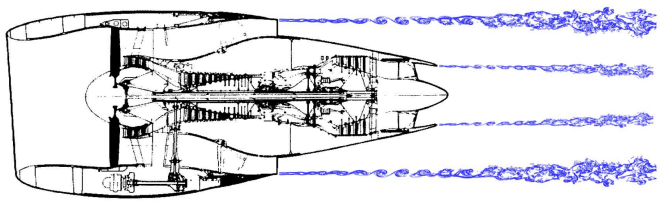

Fig. 1 Sketch of a typical bypass jet engine with the occurring mixing layers behind the nozzles.

At the beginning of the project, a high-order, low-dispersion/low-dissipation numerical scheme for the solution of the unsteady compressible Navier-Stokes equations was available [11]. However, more complex configurations and parallelization requirements lead to the development of a new DNS code. The code is embedded in a simulation framework including initial conditions, linear stability theory (LST) and postprocessing based on EAS3 [10]. The numerical scheme has been verified for aeroacoustic simulations by comparison with the benchmark problem [9]. An alternative method of handling the multiscale problem is the coupling with an acoustic

solver. Its principle functionality could be shown in cooperation with subproject 3 [2].

IMFT has gained experience in the application of optimal control theory, see e.g. [1, 19]. The application of the adjoint equations has been extended to compressible flows [17, 18]. The open-loop control with DNS is the only approach which allows to deal with some one million of unknowns for each time step. The main drawback of the open-looped control is a poor robustness due to the absence of a feedback loop. With the real flow conditions being different from the ones used to design the optimal control, at least the control law can be inefficient or may even increase the noise emission. However, as demonstrated in [18], the sensitivity analysis which can be seen as an initial step of an optimal control approach can propose some essential information about the optimality in types and in the positions of sensors and actuators for a feedback control system. With some few runs it is then possible to have a better idea of the capacity of controlling the physics of the flow.

The numerical methods used for DNS and optimal control are addressed in sections 2.1 and 2.2, respectively. The fundamental mechanisms of noise generation in a two-dimensional mixing layer are discussed in 3. Section 4 describes the optimal control applied to such a flow field. The influence of a serrated nozzle end is treated in section 5 and the emitted sound is compared to the case with a straight trailing edge.

2 Numerical Method

2.1 Direct Numerical Simulation

Direct numerical simulations are performed by the DNS-code NS3D [5] solving the unsteady three-dimensional compressible Navier-Stokes equations on multiple domains. The purpose of domain decomposition is not only to increase computational performance. The combination with grid transformation and the concept of modular boundary conditions allows to compute a wide range of problems. Computation is done in non-dimensional quantities: velocities are normalized by the reference velocity $\tilde{u}_\infty$, and all other quantities by their inflow values, marked with the subscript $_\infty$. Length scales are made dimensionless with a reference length $\tilde{L}$ and the time t with $\tilde{L}/\tilde{u}_\infty$, where the tilde denotes dimensional values. Temperature dependence of viscosity μ is modelled using the Sutherland law:

$$\tilde{\mu}(T) = \tilde{\mu}(\tilde{T}_\infty) \cdot T^{3/2} \cdot \frac{1+T_s}{T+T_s}\,, \tag{1}$$

where $T_s = 110.4K/\tilde{T}_\infty$ and $\tilde{\mu}(\tilde{T}_\infty = 280K) = 1.735 \cdot 10^{-5} kg/(ms)$. Thermal conductivity ϑ is obtained by assuming a constant Prandtl number $Pr = c_p\mu/\vartheta$. The most characteristic parameters describing a compressible viscous flow-field are the Mach number $Ma = u_\infty/c_\infty$ and the Reynolds number $Re = \rho_\infty u_\infty L/\mu_\infty$. We use the

conservative formulation of the Navier-Stokes equations which results in the solution vector $\mathbf{Q} = [\rho, \rho u, \rho v, \rho w, E]$ containing the density, the three mass fluxes and the total energy per volume:

$$E = \rho \cdot c_v \cdot T + \frac{\rho}{2} \cdot \left(u^2 + v^2 + w^2\right) . \tag{2}$$

The simulation is carried out in a rectangular domain with x, y, z being the coordinates in streamwise, normal and spanwise direction, respectively. The flow is assumed to be periodic in spanwise direction. Thus a spectral discretization is used in z-direction:

$$f(x,y,z,t) = \sum_{k=-K}^{K} \hat{F}_k(x,y,t) \cdot e^{i(k\gamma_0 z)} . \tag{3}$$

f denotes any flow variable, $\hat{F}_k$ its complex Fourier coefficient, K the number of spanwise modes and $i = \sqrt{-1}$. The fundamental spanwise wavenumber γ_0 is given by the fundamental wavelength $\lambda_{z,0}$ representing the width of the integration domain by $\gamma_0 = 2\pi/\lambda_{z,0}$.

Spanwise derivatives are computed by transforming the respective variable into Fourier space, multiplying its spectral components with their wavenumbers $(i \cdot k \cdot \gamma_0)$ for the first derivatives or square of their wavenumbers $(-k^2 \cdot \gamma_0^2)$ for the second derivatives and transforming them back into physical space. Due to the non-linear terms in the Navier-Stokes equations, higher harmonic spectral modes are generated at each time step. To suppress aliasing, only $2/3$ of the maximum number of modes for a specific z-resolution are used [7]. If a two-dimensional baseflow is used and introduced disturbances of u, v, ρ, T, p are symmetric and disturbances of w are antisymmetric, flow variables are symmetric/antisymmetric with respect to $z = 0$. Therefore only half the number of points in spanwise direction are needed ($0 \leq z \leq \lambda_z/2$), or equivalently, the $\hat{F}_k$s are either purely real or imaginary.

The spatial discretization in streamwise (x) and normal (y) direction is done by 6^{th}-order compact finite differences. The tridiagonal equation systems resulting from the compact finite differences are solved using the Thomas algorithm. To reduce the aliasing error, alternating up- and downwind-biased finite differences are used for convective terms as proposed by Kloker [15]. The second derivatives are evaluated directly which distinctly better resolves the second derivatives compared to applying the first derivative twice, see [4]. Additionally, the numerical scheme is more robust since the second derivative does not vanish for the least resolved wave. Arbitrary grid transformation in the x-y plane is provided by mapping the physical grid on an equidistant computational ξ-η grid:

$$x = x(\xi, \eta) \, , \; y = y(\xi, \eta) \, . \tag{4}$$

Time integration of the Navier-Stokes equations is done using the classical 4^{th}-order Runge-Kutta scheme as described in [15]. At each time step and each intermediate level the biasing of the finite differences for the convective terms is changed.

At the borders of each domain where no neighbor exists, specific boundary conditions can be selected. For the current investigation, we use a one-dimensional characteristic boundary condition [13] at the freestream. This allows straight outward-propagating acoustic waves to leave the domain. An additional damping zone drives the flow variables smoothly towards to a steady state solution, avoiding reflections due to oblique waves. Having a subsonic flow, we also use a characteristic boundary condition at the inflow. Additionally amplitude and phase distributions from linear stability theory can be prescribed to introduce defined disturbances. Their phase shift is defined with respect to the maximum amplitude of the streamwise velocity. The disturbances due to the eigenfunctions are added after the characteristic boundary condition is applied. Thus they are less affected by the characteristic treatment.

The outflow is the most crucial part as one has to avoid large structures passing the boundary and contaminating the acoustic field. Therefore, a combination of grid stretching and spatial low-pass filtering is applied in the sponge region. Disturbances become increasingly badly resolved as they propagate through the sponge region. As the strength of the spatial filter depends on the step size in x-direction, perturbations are smoothly dissipated before they reach the outflow boundary. This procedure shows very low reflections and has been already applied by Colonius et al. [8].

For the splitter plate representing the nozzle end, an isothermal boundary condition is used with the wall temperature being fixed to its value from the initial condition. The pressure is obtained by extrapolation from the interior gridpoints. An extension of the wall boundary condition is the modified trailing edge, where the end of the splitter plate is no more constant along the spanwise direction. As we have grid transformation only in the x-y plane and not in z-direction, the spanwise dependency of the trailing edge is achieved by modifying the connectivity of the affected domains. Instead of regularly prescribing the wall boundary condition along the whole border of the respective subdomain, we can also define a region without wall, now. At these gridpoints, the spatial derivatives in normal direction are recomputed, now using also values from the domain on the other side of the splitter plate. The spanwise derivatives are computed in the same manner as inside the flowfield with the Fourier-transformation being applied along the whole spanwise extent of the domain. Inside the notch the full equations with the newly computed y-derivateives are solved. The concept of modular boundary conditions, chosen because of flexibility and maintainability, requires explicit boundary conditions and by that a non-compact finite-difference scheme, here. Therefore explicit finite differences have been developed with properties similar to the compact scheme used in the rest of the domain. The numerical properties of the chosen 8^{th}-order scheme are compared with standard explicit 6^{th}-order finite differences and the compact scheme of 6^{th} order, regularly used in the flowfield. For the first derivative, the real and imaginary parts of the modified wavenumber k^*_{mod} are shown in figure 2: the increase from order six to eight does not fully reach the good dispersion relation of the 6^{th}-order compact scheme but at least increases the maximum of k^*_{mod} by 10% compared with an ad hoc explicit 6^{th}-order implementation. The imaginary part of the modified wavenumber, responsible for dissipation, shows similar characteristics as the compact scheme with the same maximum as for the rest of the domain.

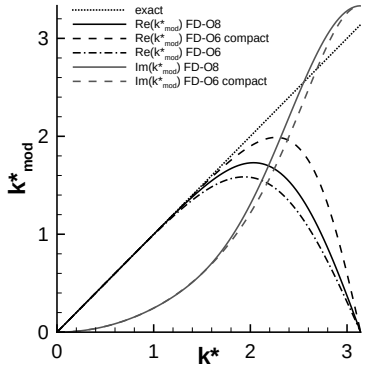

Fig. 2 Real and imaginary part of the modified wavenumber k^*_{mod} for the first derivative based on a wave with wave number $k^* = k \cdot \Delta x$. Comparison of 8^{th}-order explicit finite difference with 6^{th}-order explicit and compact scheme.

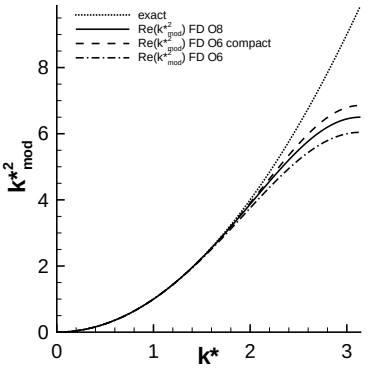

Fig. 3 Square of the modified wavenumber of the second derivative for a wave with wave number $k^* = k \cdot \Delta x$. Comparison of 8^{th}-order explicit finite difference with 6^{th}-order explicit and compact scheme.

For the second derivative, shown by the modified wavenumber square $(k^{*2})_{mod}$ in figure 3, the increase of its order improves the properties of the explicit finite difference towards the compact scheme.

2.2 Optimal Control

The uncontrolled mixing layer is computed with DNS. Some typical iso-vorticity lines at one time instance are shown in figure 4. The real computational domain (Ω) is much larger than what is shown in the figure. A line (Ω_2) located quite far from the mixing layer instabilities defines the location where the noise emission is targeted for reduction. It is called the measurement domain, usually where sensors could be positioned. Two control domains, a smaller one (Ω_{11}) and a larger one (Ω_{10}) are fixed at the birth of the mixing layer. The measurement and control domains have been determined from the previous sensitivity analysis [18, 17]. There it has been demonstrated that the noise emission, far from the mixing layer, is very sensitive to any perturbation at the origin of the mixing layer. To decrease the noise emission and for the well-posedness of the control problem we target to minimize the following objective functional:

$$J(\mathbf{f}) = \int_0^T \int_{\Omega_2} (p(\mathbf{x},t) - \overline{p}(\mathbf{x}))^2 \mathrm{d}\mathbf{x}\mathrm{d}t + \ell_0^2 \int_0^T \int_{\Omega_{1n}} \mathbf{f}^T \mathbf{B}^\mathbf{T} \mathbf{B} \mathbf{f} \mathrm{d}\mathbf{x}\mathrm{d}t \qquad (5)$$

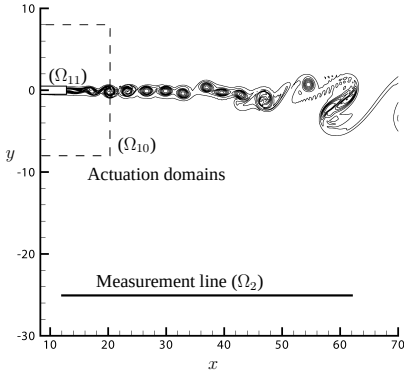

Fig. 4 Actuation domain (close to the origin o the shear layer). The line in the south of the domain is the line where the reduction of noise is targeted.

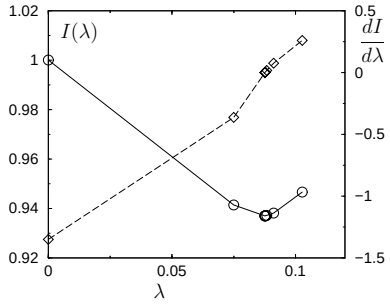

Fig. 5 Actuation domain Ω_{11}, first global iteration : $I(\lambda)$ (left scaling) and $\dfrac{dI}{d\lambda}$ (right scaling).

where $\overline{p}(\mathbf{x})$ denotes the temporal mean value of the pressure at the location $\mathbf{x}$ in the uncontrolled case. The weighted matrix $\mathbf{B}$ allows to test different types of forcing (control) by keeping only the desired components of the control vector $\mathbf{f}$. The ℓ_0 coefficient gives a bound to the control cost. Setting $\ell_0 = 0$ leads to find the most effective control without taking into account the energy cost which could theoretically go to infinity. Several numerical experiments have shown that for our case, the cost of the energy is always negligible. Hence we will set $\ell_0 = 0$ in the following for simplicity.

The minimum of the functional is obtained from an iterative procedure using a conjugate gradient algorithm. The gradient of the cost functional with respect to the control variable is calculated by a small perturbation of an associated Lagrangian functional including all the constrains: the goal, the control cost, the main Navier-Stokes equations and the boundary conditions. It can be shown [17, 19] that the Lagrange coefficient associated to the governing equations is the adjoint vector $\mathbf{r}$ of the state variables (density, momentum vector and pressure) called vector $\mathbf{q} = (\rho, m_x, m_y, p)$). The adjoint variables are solutions of the adjoint compressible two-dimensional Navier-Stokes equations [17]:

$$\mathscr{F}^*(\mathbf{q})\mathbf{r} = (p(\mathbf{x},t) - \overline{p}(\mathbf{x}))^2 \delta(\Omega_2), \tag{6}$$

with $\mathbf{r} = (p^*, m_x^*, m_y^*, \rho^*)$ as the adjoint vector and $\delta(\Omega_2)$ a function equal to 1 over Ω_2 and equal to 0 elsewhere. The source term comes from the derivative of the Lagrangian functional (eq. 5) with respect to the direct state. Finally the gradient of the Lagrangian functional with respect to the control is given by

$$\nabla J_{\mathbf{f}} = \ell_0^2 \mathbf{B}\mathbf{f} + \mathbf{r}. \tag{7}$$

When the control iterative algorithm is converged, this gradient is equal to zero and the solution provides the optimal control **f** from the adjoint state.

3 Fundamentals of Mixing-Layer Noise

3.1 Flow Parameters

The fundamental mechanisms of jet noise are investigated by considering a two-dimensional mixing layer where an S-shaped velocity profile is prescribed at the inflow. The flow parameters have been closely matched to the case of Colonius et al. [9]. This allows to validate the numerical scheme for aeroacoustic simulations. The Mach numbers of the upper and lower stream are $Ma_I = 0.5$ and $Ma_{II} = 0.25$, respectively. As both free stream temperatures are equal ($\tilde{T}_I = \tilde{T}_{II} = 280K$), the ratio of the streamwise velocities is $u_I/u_{II} = 2$. The Reynolds number $Re = \rho_I u_I \delta(x_0)/\mu = 500$ is based on the vorticity thickness at the inflow which is used to normalize length scales. A cartesian grid is used with 2500x850 grid points in x- and y-direction. In streamwise direction, the grid is uniform with spacing $\Delta x = 0.157$ up to the sponge region where the grid is highly stretched. In normal direction, the grid is continuously stretched with the smallest stepsize $\Delta y = 0.15$ in the middle of the mixing layer and the largest spacing $\Delta y = 1.06$ at the upper and lower boundaries. In case of the three-dimensional simulation, the z-direction is discretized with 9 grid points and $\Delta z = 0.491$. This is equivalent to 10 spanwise modes (dealiased) with $\gamma_0 = 0.8$ in the symmetric case.

The initial condition, obtained from the similarity solution of the boundary-layer equations, is used for linear stability theory. The most amplified disturbance is found for the fundamental frequency $\omega_0 = 0.6293$ at the inflow. The eigenfunctions from linear stability theory are used to introduce defined disturbances at the inflow. The flow is forced with the fundamental frequency and its first three subharmonics ($1/2$, $1/4$ and $1/8$) with the maximum of $|\hat{u}| = 0.001$ for all disturbances. The phase shift is $\Delta\Theta = -0.028$ for the first, $\Delta\Theta = 0.141$ for the second subharmonic and $\Delta\Theta = 0.391$ for the third subharmonic. In an additional simulation the phase shift of $\omega_0/4$ is altered to $\Delta\Theta = 3.141$. Note that it is not clear how the phase shift is specified in [9] since the phase distribution varies along the normal direction. Here it is defined with respect to the maximum of $|\hat{u}|$ such that $\Theta = 0$ at the location of $|\hat{u}|_{max}$ in case of no phase shift. An additional steady disturbance $(0,1)$ with amplitude $|\hat{u}| = 0.01$ is introduced in the three-dimensional simulation with $\Delta\Theta = 3.141$. The modes are denoted as (h,k), with h and k being the multiple of the fundamental frequency ω_0 and the spanwise wavenumber γ_0, respectively.

3.2 Two-Dimensional Simulation

The spanwise vorticity is shown in figure 6 being similar to the reference solution of Colonius et al. [9]. Since eigenfunctions from viscous linear stability theory instead of inviscid ones as used in [9] are used here, disturbances are introduced slightly more efficient. Accordingly the rollup of the mixing layer and the vortex pairing occur a bit earlier.

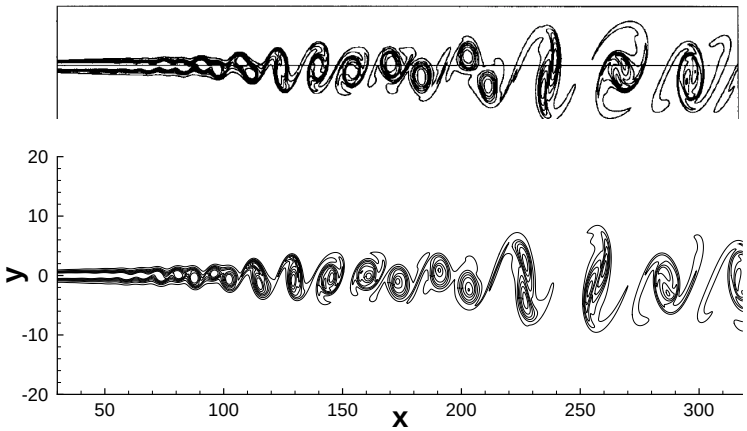

Fig. 6 Snapshot of the spanwise vorticity for $\Delta\Theta(\omega_0/4) = 0.141$ after 76 fundamental periods. Contour levels range from -0.26 to 0.02 with an increment of 0.04. The reference solution of Colonius et al. [9] is shown above.

The maximum amplitudes of the normal velocity v along the y-direction and the corresponding amplification rates are shown in figures 7 and 8, respectively. In the initial region of the integration domain the amplitudes grow exponentially. Despite the spatial amplification rate $(-\alpha_i)$ is a very sensitive value, its values correspond well to those of linear stability theory. Further downstream, modes $(1,0)$, $(1/2,0)$, $(1/4,0)$ saturate at positions $x = 90$, $x = 120$ and $x = 240$, respectively. These streamwise locations correlate well with the positions where the respective vortices are fully developed (figure 6). At the location where $(1/2,0)$ and $(1/4,0)$ saturate ($x = 120$ and $x = 240$), the growth of the respective subharmonics $(1/4,0)$ and $(1/8,0)$ is interrupted before their amplitude increases again.

The alternative phase shift $\Delta\Theta(\omega_0/4) = 3.141$ does not affect the initial growth of the amplitudes as shown in figure 9. Yet the development of the second subharmonic differs from $x \approx 120$ onwards. There, its phase is adjusted to the one of the first subharmonic. This can be seen in figure 10 showing the phase speed $c_{ph} = \omega \cdot (\partial\Theta/\partial x)^{-1}$ of the first two subharmonics at $y = 0$. Phase adjustment is found for both cases, but for $\Delta\Theta(\omega_0/4) = 3.141$, the phase speed varies more and subharmonic resonance of mode $(1/4,0)$ is achieved with a reduced amplitude com-

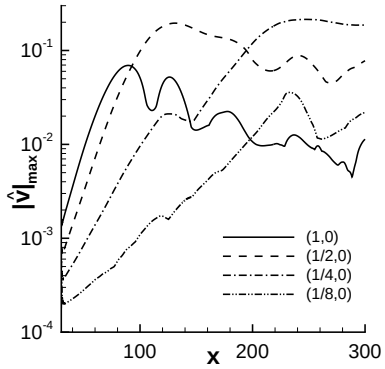

Fig. 7 Maximum amplitudes of the normal velocity v along y-direction for $\Delta\Theta(\omega_0/4) = 0.141$.

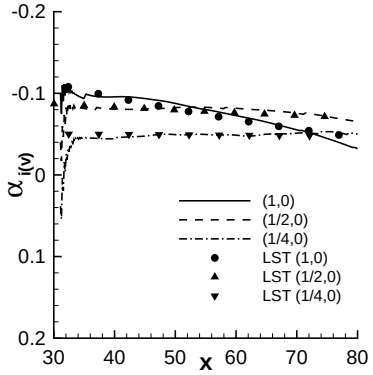

Fig. 8 Amplification rates of the normal velocity v for $\Delta\Theta(\omega_0/4) = 0.141$. Symbols denote results from linear stability theory.

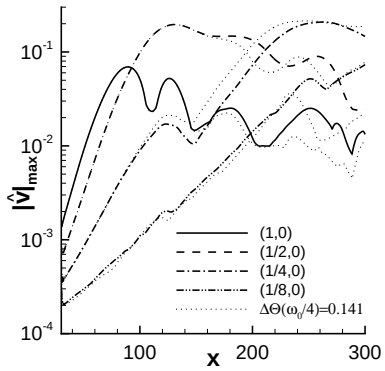

Fig. 9 Maximum amplitudes of the normal velocity v along y-direction for $\Delta\Theta(\omega_0/4) = 3.141$. Dotted lines denote the previous case with $\Delta\Theta(\omega_0/4) = 0.141$.

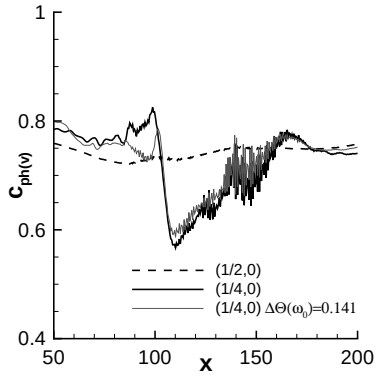

Fig. 10 Phase speed c_{ph} of the normal velocity v at $y = 0$ compared with the prevoius case.

pared to $\Delta\Theta(\omega_0/4) = 0.141$. Accordingly, its saturation is further downstream and faster resonance of the third subharmonic is provided. This leads to an increased amplitude of $(1/8,0)$ by a factor of almost four downstream of $x \geq 270$.

The acoustic field is visualized by the dilatation which is the divergence of the velocity field $\nabla \cdot \mathbf{u}$. For both 2-d simulations, the sound with frequency $\omega_0/2$ is emitted from $x \approx 120$, being the position of the first vortex pairing. Both, intensity and directivity show good agreement with the reference solution of Colonius et al. [9]. In case of $\Delta\Theta(\omega_0/4) = 0.141$, the sound with frequency $\omega_0/4$ is emitted

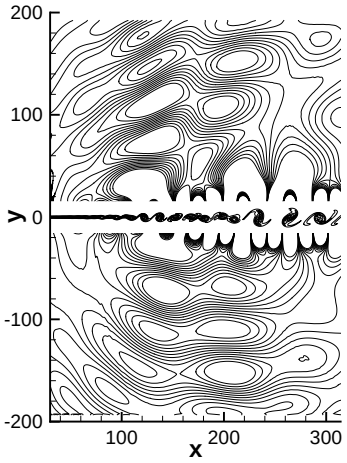

Fig. 11 Emitted sound with frequency $\omega_0/4$, visualized by the real part of the Fourier-transformed dilatation with contour levels ranging from $-2 \cdot 10^{-6}$ to $2 \cdot 10^{-6}$ for $\Delta\Theta(\omega_0/4) = 0.141$

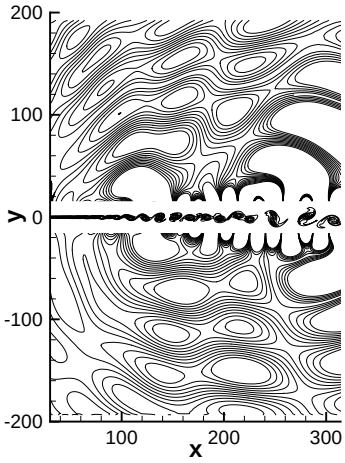

Fig. 12 Real part of the Fourier-transformed dilatation field with frequency $\omega_0/4$ for $\Delta\Theta(\omega_0/4) = 3.141$. Contour levels are the same as in figure 11.

mainly perpendicular to the flow direction as shown in figure 11. With the alternative disturbance of mode $(1/4, 0)$, the emitted sound is more intense and is directed mainly in downstream direction. The latter case corresponds to the results of [9] and [4].

3.3 Three-dimensional Simulation

The quite high amplitude of the introduced mode $(0, 1)$ allows two-dimensional disturbances to interact with, generating unsteady oblique disturbances. The initial growth of the two-dimensional disturbances is similar up to the saturation of the first subharmonic as shown in figure 13. Non-linear interaction of the steady disturbance $(0, 1)$ with two-dimensional instability waves rapidly genrates oblique modes, shown in figure 14. At $x \approx 130$, disturbances $(1, 1)$ and $(1/2, 1)$ reach a level of $|\hat{v}| \approx 5 \cdot 10^{-5}$. The increased amplitudes of the oblique modes come up with a large amplitude of the steady mode $(0, 1)$. This inhibits the growth of the second subharmonic $(1/4, 0)$), known from the corresponding two-dimensional case. As shown by the phase speed given in figure 15, the phase of the second subharmonic $(1/4, 0)$ is not able to adapt to the dominant disturbance and its resonance is prevented.

For this case, the spanwise vorticity at the symmetry plane $z = 0$ is shown in figure 16. The initial region is similar to the two-dimensional simulations: the mix-

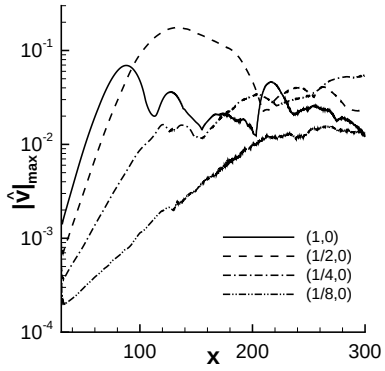

Fig. 13 Maximum amplitudes of the normal velocity v of 2-d modes $(h,0)$.

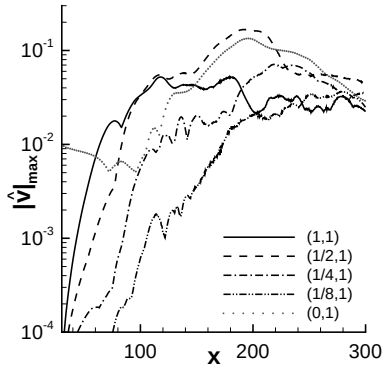

Fig. 14 Three-dimensional disturbances $(h,1)$ of the maximum amplitude of v.

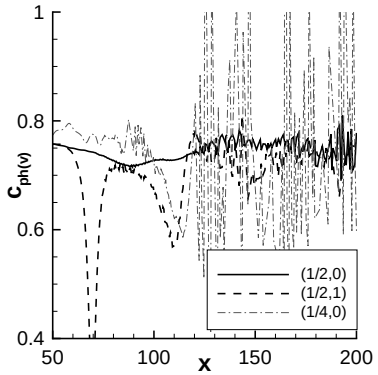

Fig. 15 Phase velocities of the first and second subharmonics, based on the normal velocity at $y = 0$.

ing layer rolls up into vortices and the first pairing takes place at $x \approx 120$. Further downstream three-dimensional effects increase and the vortical structures differ. The vortices break up into small-scale structures for $x > 150$. Compared to figure 6, large scales almost disappear.

The emitted sound with frequency of the second subharmonic is shown in figure 17. Compared to the corresponding two-dimensional case of figure 12, a sound reduction by roughly two is observed in the lower half of the domain. An additional source is located at $x \approx 130$. Thus, the emitted sound in upstream direction is due to the suppressed resonance of mode $(1/4,0)$. The acoustic source at $x \approx 220$ is not tonal but emits broad-band noise. This is shown exemplarily for the undisturbed frequency $3/4 \cdot \omega_0$ in figure 18.

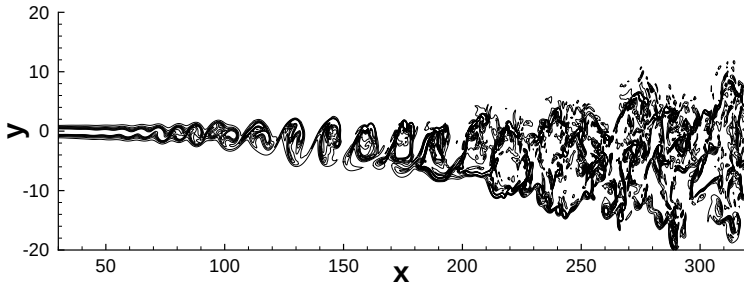

Fig. 16 Snapshot of the spanwise vorticity for the three-dimensional simulation at the symmetry plane $z = 0$. Contour levels correspond to those of figure 6

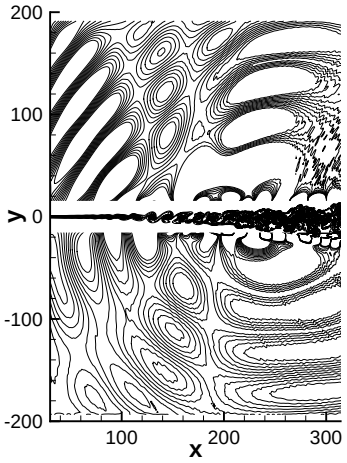

Fig. 17 Emitted sound with frequency $\omega_0/4$, visualized by the real part of the Fourier-transformed dilatation with contour levels ranging from $-2 \cdot 10^{-6}$ to $2 \cdot 10^{-6}$ for $\Delta\Theta(\omega_0/4) = 0.141$

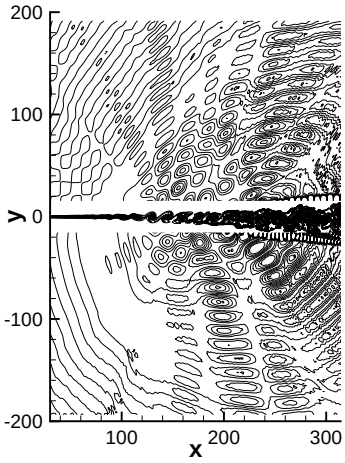

Fig. 18 Real part of the Fourier-transformed dilatation field of the undisturbed frequency $3/4 \cdot \omega_0$ with the same contour levels as on the left side.

The above results show that subharmonics play an important role in the mechanism of sound generation. A varied phase shift can alter the process of subharmonic resonance and thus the major part of the generated noise. The resonance of two-dimensional modes can be suppressed by a spanwise moculation of the flow.

4 Optimal Control of Mixing-Layer Noise

4.1 Computational Aspects

A non uniform mesh with 601×501 nodes has been designed to improve accuracy in the mixing layer. The grid is uniform in the x-direction up to a given value x_p which corresponds to the size of the physical box. Then the streamwise step size Δx is increases successively up to the outflow boundary of the computational domain where the step size is $\Delta x_{final} \approx 300\Delta x_0$. This is a simple way for filtering undesired upstream convected structures, coming from possible numerical wave reflection from the outlet boundary.

The boundary conditions in the north, south and east frontier of the computational domain are given from the characteristic theory [16]. They allow the exit of acoustic and entropy waves, limiting reflections.

At the west frontier, the inlet of the domain, the flow is excited by its highest unstable eigenmode, given by linear stability theory. Its frequency is $\omega_0 = 1.226$. Forcing the flow at this location by its eigenmode decreases drastically the numerical transient behavior and increases the convergence speed.

The upper flow velocity is the reference velocity with a Mach number $Ma_I = 0.8$. The Mach number of the lower stream is $Ma_{II} = 0.2$. The reference temperature is set to $T_0 = 280K$. The reference length L is given from a Reynolds number of $R = 2500$. It corresponds to a shear layer thickness of δ given by $\delta/L = 0.3738$ at the inlet of the computational domain. The total duration of the simulation is $t_{end} = 51.24$ being 10 periods of the introduced instability, calculating over 10240 time steps.

The gradient of the Lagrangian functional is determined from the direct simulation of the adjoint Navier-Stokes equation. The design of the adjoint code is very similar to the one of the direct state simulation. Non-reflecting boundary conditions based on the characteristic theory are also proposed to prevent numerical errors in the dual (adjoint) space. Note that incoming and outcoming characteristics are inverted between the direct and adjoint equations. A buffer zone is added in the dual space upstream of the computational domain used in the direct calculations, in the same way as the one existing downstream in the physical domain. Wave propagation is very similar in physical and in dual space. The location of the new buffer zone is explained by the fact that adjoint equations are integrated backward in time.

The optimal control is obtained after approximately 5 to 7 global iterations. During each global iteration, the gradient of the cost functional is given from a conjugate-gradient algorithm which requires itself 10 iterations of the direct-adjoint simulations of the Navier-Stokes equations.

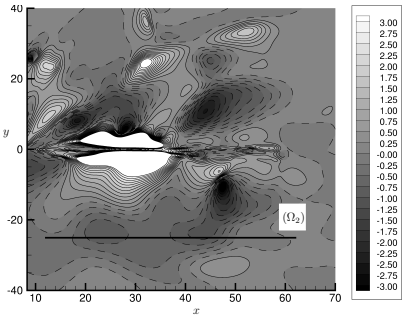

Fig. 19 Difference of acoustic pressure level (SPL) between the actuated case with a mass forcing and the unactuated case, in dB. The measurement line Ω_2 is in the lower part of the domain.

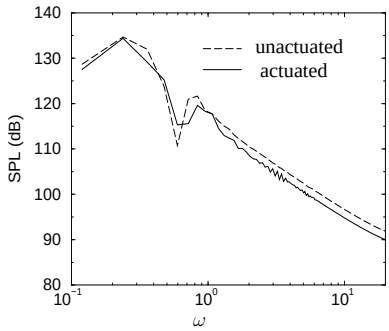

Fig. 20 Acoustic spectrum at the location $(43.5, -25)$ in the actuated and unactuated case.

4.2 Simulation Results

The adjoint simulations have been validated with a sensitivity analysis [18]. Since the adjoint variables are also gradients of the cost functional, it is possible to compare the evolution of the variation of a non-dimensional cost functional $I = J_n/J_0$ and its gradient given by the adjoint quantity (eq. 7). It has been verified on figure 5 where the index on the horizontal axis is the index of the global iterations. λ is the parameter (or variable) usually used in the conjugate gradient algorithm which determines the steepest descent direction. The evolution of the functional and its derivatives correspond perfectly, especially the minimum is reached when the gradient (from adjoint equations) is given as null. In this case, the control is a source term in the continuity equation and it can be interpreted as some injection of mass on the larger actuation domain named (Ω_{11}). The minimum found by the algorithm corresponds to a 10,4 % decrease of the functional after 5 global iterations. The mean noise reduction over the horizontal line (measurement line) is 0.5dB. It is weak compared to the previous work of Wei and Freund [20] where a reduction of 3dB was reached after 4 global iterations. Following Wei and Freund's conclusions the actuation subtly modifies the small space and time scales of the flow in such a way that general organization is improved from an aeroacoustic viewpoint. The discrepancy between the success of the control in the two studies is explained as follows. In [20], the inlet boundary condition is the sum of the fundamental eigenmode and three harmonics. These 4 modes are perturbed randomly in the frequency domain and in amplitudes. Such an approach artificially increases the noise emission. The role of the final control is then to reduce the noise, and it happens that such artificial noise is canceled. Since we introduce just the fundamental mode without random perturbation the initial noise level is weak in our test case. Thus the actuation has

less work to do, since the flow is well organized. Another point is that we have the Mach number $Ma_I = 0.8$ instead of 0.9 in [20], being initially more noisy.

The difference of the sound pressure level (SPL) between the actuated and the unactuated flow is shown in figure 19. The decrease is not important on the measurement line (Ω_2) where noise reduction was targeted, but a reduction of 3dB is reached in other locations in the shear layer. In an opposite way, some local 3 dB increase of noise level can be observed, but the noise seems not to propagate but to stay localized. Finally, noise control appears effective in a larger part of the flow, outside of the targeted line. This mean global reduction is not discussed in [20].

An analysis of the pressure spectrum has been performed. We chose to calculate the spectrum at a point on the measurement line Ω_2 of coordinates $(43.5, -25)$ with the largest noise reduction. The spectra in the actuated and unactuated case are presented in figure 20. A local minimum at a reduced frequency $\omega_0 \approx 0.61$ is shown in the unactuated spectrum. This could be a subharmonic at frequency $\omega_0/2$ of the initial fundamental mode. Even if the reduction is weak, actuation plays a positive role in a broad band of frequency, except close to $\omega_0 \approx 0.61$ where noise emission is increased. Actuation seems to regularize the acoustic spectrum. This broadband effect should be investigated more closely in the future.

A Principal Component Analysis (PCA) of the control function (actuation mode) has been used to compare with the conclusions of Wei and Freund [20]. It is a singular value decomposition following a Karhunen-Love transform, also known as Proper Orthogonal Decomposition (POD). The actuation is decomposed as

$$\mathbf{f}(\mathbf{x},t) = \sum_{i=1}^{N} \lambda_i(t)\Phi_i(\mathbf{x}). \tag{8}$$

Details can be found in [17]. The first mode is dominant and 55.7 % of the energy is contained in the first two modes. There is a discrepancy with the previous work [20] where 10 modes are necessary to provide 50 % of the total energy. The structure of the actuation is less simple in our study than in Wei's flow. However, similar to Wei's conclusion, the modes are essentially spatially distributed around the mixing layer and the characteristic length scale decreases with the rank of the mode but remains in the same order of magnitude. This agreement confirms that the control essentially acts on some large scale, deeply modifying the flow structure.

Simultaneous actuation on the fourth equation of the Navier-Stokes model has weakly increased the efficiency of the control, since a noise reduction of 0.6 dB has been pointed out. The conclusions given above are always valid but the area of local increase or decrease of noise emission are larger than in the previous case. The actuation on the whole Navier-Stokes equations is not so different from a unique actuation by injection of mass. It only confirms that the highest sensitivity of the noise emission is a mass source [18]. Spectrum and PCA analysis just support this conclusion. Some studies where the actuation domain was small (called Ω_{10} on figure 4) have demonstrated that noise reduction can be difficult or even might be impossible when the distribution of the control is too restrictive. This seems to be a limit of the open-loop control approach.

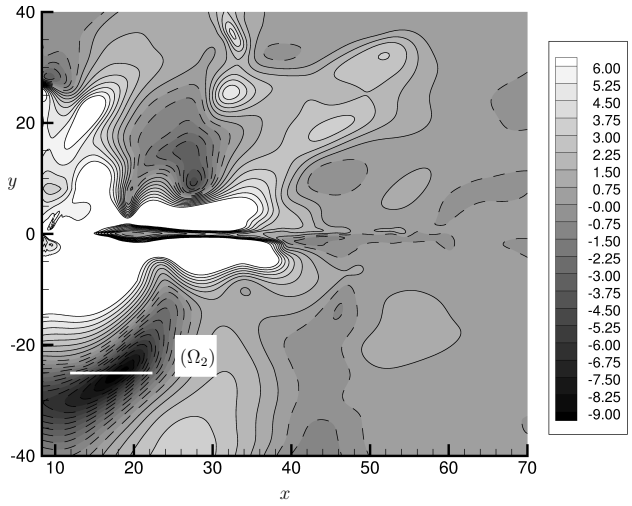

Fig. 21 Difference of the acoustic level (SPL) between the actuated and the unactuated case in dB (control on the fourth component of the Navier-Stokes equations). The measurement line Ω_2' is in white, at $y = -24$

If the measurement line is small (white line Ω_2' on fig. 21) and the actuation domain is the larger one, a larger noise reduction of 6 dB has been reached with 6 global iterations in the control algorithm. As in the previous example, locally a reduction or an increase of 9 dB can be seen in some parts of the physical domain. However, globally and far from the mixing layer a mean reduction is conserved. The Principal Component Analysis has shown that with a small size of the targeted line which is quite far away from the noise emission, the optimal control approach provides an anti-noise control. The actuation acts as a wave which arrives at the small measurement line (approximately seen as a point) with an opposite phase and with the same amplitude as the wave which arrives at the same location but in the unactuated case. The actuation is more effective since the noise to be reduced is concentrated in a small area and the final goal is easier than the reduction of noise on a long line.

5 Serrated Nozzle End

5.1 Flow Parameters

The nozzle end of a jet is modelled by a finite flat splitter plate with two-different free-stream velocities above and below. The Mach numbers $Ma_I = 0.8$ for the up-

per and Ma_{II} for the lower stream have been chosen according to chapter 4. Again the free-stream temperatures are equal ($\tilde{T}_I = \tilde{T}_{II} = 280K$), leading to a ratio of the streamwise velocities $u_I/u_{II} = 4$. The Reynolds number $Re = \rho_\infty U_1 \delta_{1,I}/\mu_\infty = 1000$ is based on the displacement thickness $\delta_{1,I}$ of the upper stream at the inflow. With $\delta_{1,I}(x_0) = 1$, length scales are normalized with the displacement thickness of the fast stream at the inflow. The boundary layer of the lower stream corresponds to the same origin of the flat plate.

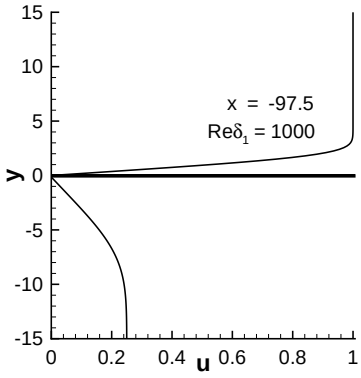

Fig. 22 Streamwise velocity profiles of the baseflow at the inflow (similarity solution of the BL equations).

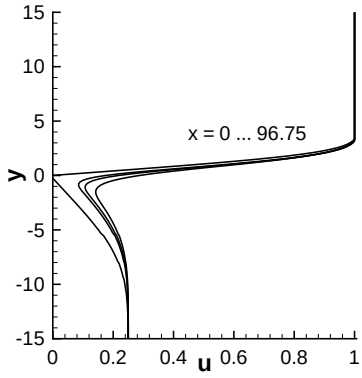

Fig. 23 Combination of wake and mixing layer behind the thin splitter plate, obtained from downstream integration of the BL equations.

The cartesian grid is made of sixteen subdomains: eight in streamwise and two in normal direction. Each subdomain contains 325 x 425 x 65 points in *x*-, *y*- and *z*-direction, resulting in a total number of 143.6 million gridpoints. The origin of the coordinate system ($x = 0$, $y = 0$) is located at the end of the nozzle end. Since the flow is symmetric to $z = 0$, the spanwise resolution corresponds to 42 spanwise modes (dealiased). The fundamental spanwise wave number is $\gamma_0 = 0.2$, where $\Delta z = 0.2454$ and $\lambda_z/2 = \pi/\gamma_0 = 15.708$ is the spanwise extent of the domain. The mesh is uniform in streamwise direction with a step size of $\Delta x = 0.15$ up to the sponge region, where the grid is highly stretched. The inflow is located at $x = -97.5$ and from $x = 250$ on, the mesh is smoothly stretched. In normal direction, the finest step size is $\Delta y = 0.15$ in the middle of the domain with a continuous stretching up to a spacing of $\Delta y = 1.06$ at the upper and lower boundaries. Due to the tiny thickness $\Delta y = 0.15$ of the splitter plate, an isothermal boundary condition at the wall has been chosen. The temperature of the plate is $\overline{T}_{wall} = 296K$, being the mean value of the adiabatic wall temperatures of the two streams.

The initial condition along the flat plate is obtained from similarity solutions of the boundary-layer equations, given in figure 22. Further downstream, the full boundary-layer equations are integrated downstream, providing a flow-field suffi-

cient to serve as an initial condition and for linear stability theory. To avoid a peak of the normal velocity near the trailing edge, it is smoothed there. Since linear stability theory does not account for the wallnormal velocity, this modification does not affect its results. As shown in figure 23, the flow field keeps its wake-like shape for a long range. As high amplification rates occur here, the flow is already unsteady before a pure mixing layer has developed.

5.2 Linear Stability Theory

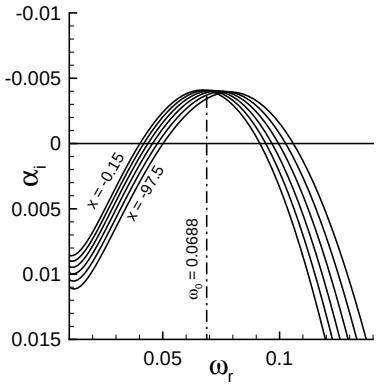

Fig. 24 Spatial amplification rates from LST in the upper boundary layer.

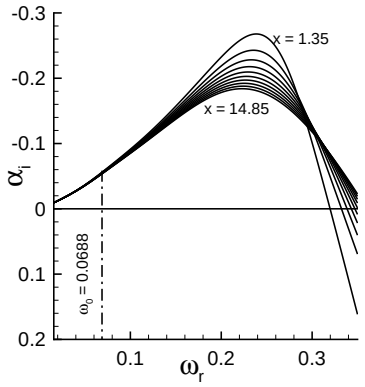

Fig. 25 Stability diagram behind the splitter plate.

The stability diagram for two-dimensional disturbances in the upper boundary layer is shown in figure 24. In accordance to the maximum amplification, the fundamental frequency $\omega_0 = 0.0688$ is chosen. In the boundary layer, the amplification rate is only weakly dependent on the streamwise position. As the two boundary layers emerge from the same position, the lower boundary layer is stable up to the nozzle end. Behind the splitter plate, amplification rates 50 times higher than in the upper boundary layer occur due to the inflection points of the streamwise-velocity profile. Maximum amplification in the mixing layer takes place for a frequency of roughly three to four times of the fundamental frequency of the boundary layer as illustrated in figure 25.

5.3 Simulation Results

The upper boundary layer is forced with the two-dimensional Tollmien-Schlichting (TS) wave $(1,0)$ with an amplitude of $|\hat{u}| = 0.005$ and an additional oblique wave pair $(1,1)$ with $|\hat{u}| = 0.0005$. Within this simulation, a rectangular serration with one notch per spanwise wavelength and a depth of 10 is considered. For the straight trailing edge, three-dimensional effects are less important and the reader is referred to [3].

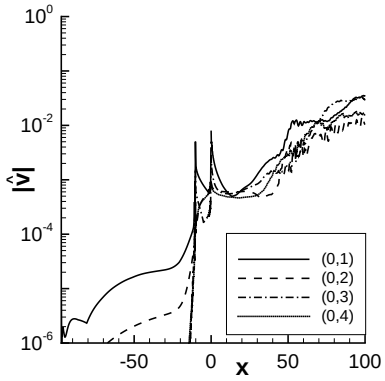

Fig. 26 Maximum amplitude of the normal velocity v for steady modes $(0,k)$.

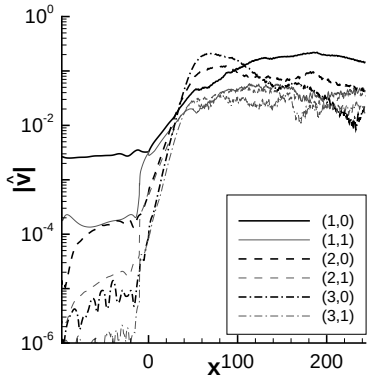

Fig. 27 Maximum amplitude of the normal velocity v for unsteady modes $(h,0)$ and $(h,1)$.

A spectral decomposition is shown in figures 26 and 27, based on the maximum of v along y. The normal velocity has been chosen as it is less associated with upstream propagating sound. In the upper boundary layer, non-linear interaction of the introduced disturbances $(1,0)$ and $(1,1)$ generates the steady mode $(0,1)$ up to an amplitude of $|\hat{v}| = 2 \cdot 10^{-5}$ (figure 26). From $x = -25$ onwards, this is exceeded by the upstream effect of the engrailment. The serrated trailing edge ($-10 \leq x \leq 0$) generates steady spanwise disturbances $(0,k)$ up to $|\hat{v}| = 8 \cdot 10^{-3}$. In the notch, the combination of wake and mixing layer originates further upstream, which corresponds to the steady spanwise mode $(0,1)$. Its amplitude decreases behind the trailing edge up to $x = 15$. Higher harmonics in spanwise direction $(0,2)$ and $(0,4)$ are generated at the notch as well, staying almost constant behind the splitter plate.

Figure 27 shows that the TS-wave generates higher harmonics in the upper boundary layer. With an amplitude of the driving TS-wave of $|\hat{v}| = 2 \cdot 10^{-3}$, modes $(2,0)$, $(3,0)$ reach amplitudes of $|\hat{v}| = 3 \cdot 10^{-4}$ and $|\hat{v}| = 2 \cdot 10^{-3}$, respectively. The increased steady modes at the engrailment interact with the two-dimensional waves, generating unsteady oblique modes $(h,1)$. Behind the splitter plate, the first two higher harmonics are growing stronger than the fundamental disturbance. Saturation

is found at $x \approx 70$ and $x \approx 160$ for the higher harmonics and mode $(1,0)$, respectively. With relevant amplitudes of the oblique waves, these disturbances grow similarly to their two-dimensional counterparts and saturate at a level of $|\hat{v}| \approx 4 \cdot 10^{-2}$. Non-linear interaction of modes $(h,1)$ creates steady modes $(0,k)$. As figure 26 shows, this exceeds the direct effect of the notch at $x \approx 15$ and $x \approx 35$ for mode $(0,1)$ and its higher harmonics, respectively.

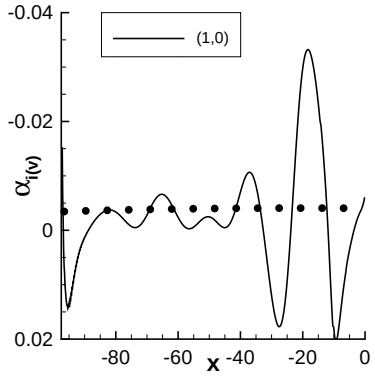

Fig. 28 Amplification of the TS-wave in the upper boundary layer, compared with LST (symbols).

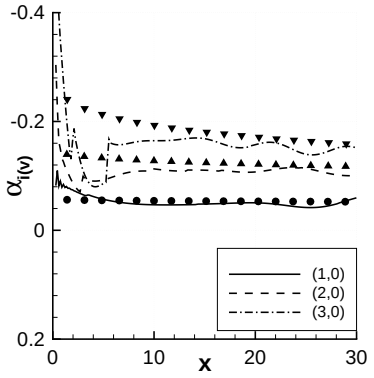

Fig. 29 Spatial amplification rates of 2-d disturbances behind the trailing edge. Symbols denote results from LST.

The spatial growth rates are compared with linear stability theory in figures 28 and 29. In the upper boundary layer, good agreement is observed. However a superimposed variation with wavelength $\lambda_x \approx 20$ is visible. This is equivalent to a phase speed $|c_{ph}| = 0.22$ which corresponds to the upstream propagating acoustic wave with $c_{ph} \approx 1 - 1/Ma_I = -0.25$. Hence the difference to LST is caused by the emitted noise of the mixing layer and not due to the three-dimensional geometry. Good agreement with LST is observed for the fundamental disturbance $(1,0)$ behind the splitter plate. Yet higher frequencies show a slightly lower mean amplification compared to linear stability theory.

Figure 30 shows an instantaneous view of the vortical structures, visualized by the isosurface of the Λ_2 vortex criterion [14]. Due to the earlier beginning of the mixing layer in the notch a spanwise deformation of the Kelvin-Helmholtz vortices occurs. At $x = 50$, the croissant-shaped vortex is still one coherent structure. The strong spanwise gradients lead to streamwise vortices which are twisted around the spanwise eddies. This leads to an early breakdown of the large spanwise rollers. Further downstream, the Kelvin-Helmholtz vortices known from dominantly two-dimensional cases, e.g. [3], are now an accumulation of small-scale structures.

The acoustic field is visualized by the real part of the Fourier-transformed dilatation field. The emission with the fundamental frequency is compared with the straight trailing edge in figure 31. The engrailed nozzle end leads to a notable re-

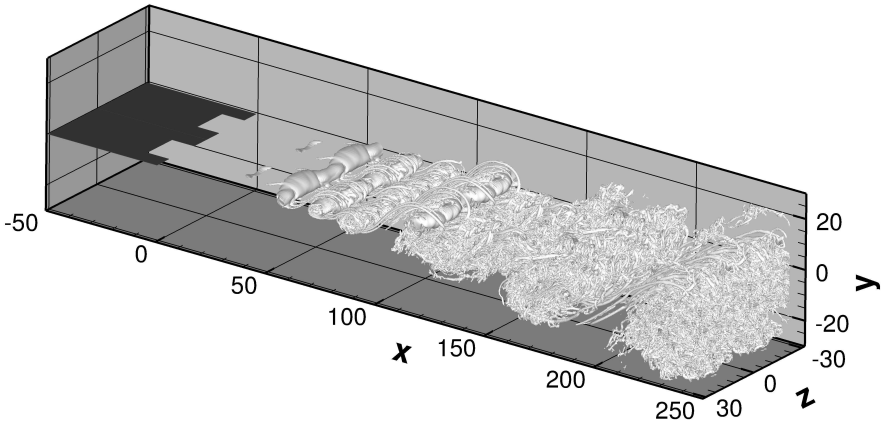

Fig. 30 Snapshot of vortical structures behind the engrailed splitter plate along two spanwise wavelengths, visualized by the isosurface $\Lambda_2 = -0.005$.

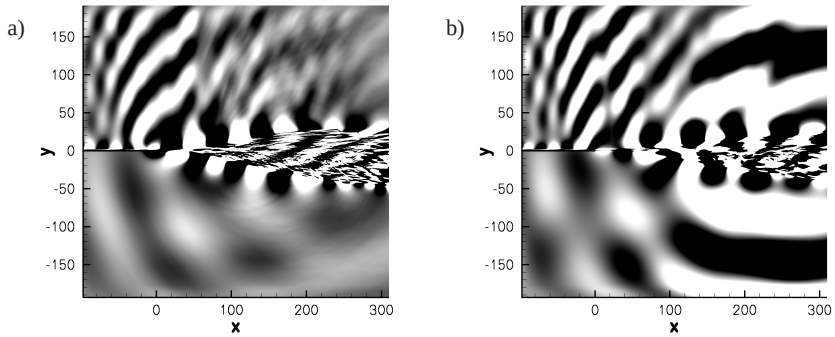

Fig. 31 Real part of the Fourier-transformed dilatation field at the symmetry plane $z = 0$ for ω_0: a) engrailment, b) straight trailing edges. Contour levels are in the range of $\nabla\mathbf{u} = \pm 3 \cdot 10^{-3}$.

duction of the generated noise which propagates in downstream direction. In both cases an upstream emission originates from $x \approx 50$ in the upper half of the domain. Its characteristic corresponds to the one due to the suppressed resonance in figure 17 for the pure mixing layer. Hence this emission is due to the phase adaptation for resonance or its suppression, respectively. The acoustic field with frequency $7/4 \cdot \omega_0$ is illustrated in figure 32 where the emitted sound is reduced as well. For both geometries, its main source is located at $x \approx 140$.

For a more quantitative evaluation of the generated sound, a virtual microphone is placed at ($x = 195$, $y = -121.8$, $z = 0$). At this position, a detailed time record is taken along 8 periods of the fundamental frequency. The temporal Fourier-analysis of the pressure fluctuations is given in figure 33 for the straight and the serrated trailing edge. The main reduction is found for frequencies up to the third higher har-

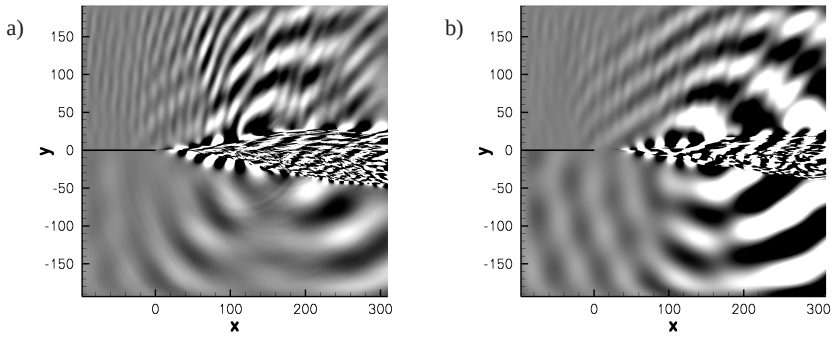

Fig. 32 Same as figure 31 but for frequency $7/4 \cdot \omega_0$: a) engrailment, b) straight trailing edges.

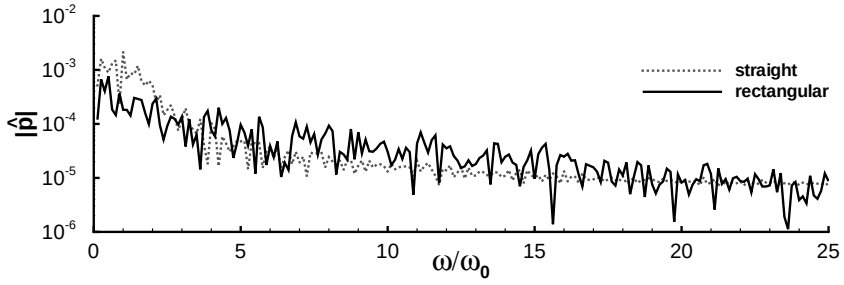

Fig. 33 Acoustic spectrum of the pressure at the virtual microphone ($x = 195$, $y = -121.8$, $z = 0$) for the rectangular engrailment and a straight trailing edge.

monic. For high frequencies, the sound spectrum decays. The overall sound-pressure level is $p'_{rms} = 0.003047$ and $p'_{rms} = 0.00108$ for the straight and the serrated trailing edge, respectively. Thus the rectangular engrailment reduces the sound pressure level by 9dB.

6 Conclusions

A numerical scheme for direct numerical simulation including direct sound computation has been developed and verified by comparing with linear stability theory and the benchmark problem of Colonius et al. [9]. The existence of a markable subharmonic could be identified as the main acoustic source in a mixing layer. Accordingly it is possible to reduce the emitted sound by a varied phase shift of the introduced particular subharmonic. An additional spanwise mode with high amplitude is capable to inhibit the resonance mechanism. Three-dimensional effects lead

to a broad-band emission of noise instead of the tonal noise of a two-dimensional mixing layer.

Optimal control of noise emission in a mixing layer has been successfully carried out. The methodology of DNS plus Adjoint DNS plus conjugate gradient algorithm works with efficiency. Depending on the size of the targeted area for noise reduction, a small or a significant decrease of the local noise level has been reached. Globally, far from the mixing layer, the mean noise level always decreases. The principal component analysis has shown two kind of actuation: some distributed control for a large measurement area and some anti-noise control for a small measurement area.

Including the nozzle end, modelled by a thin splitter plate, provides a more realistic configuration of the flow field. Additionally, it allows to investigate possible actuators directly at the wall and forcing terms inside the flow field can be avoided. In this context, passive control by a rectangular engrailment of the trailing edge has been investigated. The resulting spanwise modulation of the Kelvin-Helmholtz vortices leads to a breakdown of the coherent structures further downstream. This simple modification of the geometry showed a noise reduction of 9dB.

The next step is to add the splitter plate in the optimal control algorithm, too. Future direct numerical simulations will focus on various actuators at the splitter plate. This includes various shapes of the trailing edge as well as active actuators. One possible strategy can be the forcing of the most amplified frequency and its subharmonics. Optimizing the phase shifts may prevent the resonance mechanism accordingly to the pure mixing layer. Further simulations with larger Reynolds numbers are planed, where one or both boundary layers along the splitter plate are turbulent. This will be realized by a turbulent inflow, prescribing time-dependent quantities from previous simulations. Due to the flexibility of the DNS-code, it can be applied to other geometrical configurations as well, e.g. a complete airfoil at a low to moderate Reynolds numbers is conceivable.

Acknowledgments

The authors would like to thank the Deutsche Forschungsgemeinschaft (DFG) and the Centre National de la Recherche Scientifique (CNRS) for its financial support of the subproject SP5 in the DFG/CNRS research group FOR-508 *"Noise Generation in Turbulent Flows"*. The provision of computer resources by the Höchstleistungsrechenzentrum Stuttgart (HLRS) within the projects *"Lamtur"* and *"Teraflop Workbench"* and by IDRIS, Orsay, France is gratefully acknowledged.

References

1. C. Airiau. Non-parallel acoustic receptivity of a blasius boundary layer using an adjoint approach. *Flow, Turb. Comb.*, 65:347–367, 2000.

2. A. Babucke, M. Dumbser, and J. Utzmann. A coupling scheme for direct numerical simulations with an acoustic solver. In *CEMRACS 2005 - Computational Aeroacoustics and Computational Fluid Dynamics in Turbulent Flows*, volume 16 of *ESAIM Proc.*, pages 1–15, 2007.
3. A. Babucke, M. J. Kloker, and U. Rist. Numerical investigation of flow-induced noise generation at the nozzle end of jet engines. In *New Results in Numerical and Experimental Fluid Mechanics VI*, Contributions to the 15. STAB/DGLR Symposium Darmstadt, pages 413–420, 2007.
4. A. Babucke, M. J. Kloker, and U. Rist. DNS of a plane mixing layer for the investigation of sound generation mechanisms. *Computers and Fluids*, 37(4):360–368, 2008.
5. A. Babucke, J. Linn, M. Kloker, and U. Rist. Direct numerical simulation of shear flow phenomena on parallel vector computers. In *High performance computing on vector systems: Proceedings of the High Performance Computing Center Stuttgart 2005*, pages 229–247. Springer Verlag Berlin, 2006.
6. C. Bogey, C. Bailly, and D. Juve. Numerical simulation of sound generated by vortex pairing in a mixing layer. *AIAA J.*, 38(12):2210–2218, 2000.
7. C. Canuto, M. Y. Hussaini, and A. Quarteroni. *Spectral methods in fluid dynamics*. Springer Series of Computational Physics. SpringerVerlag Berlin, 1988.
8. T. Colonius, S. K. Lele, and P. Moin. Boundary conditions for direct computation of aerodynamic sound generation. *AIAA Journal*, 31(9):1574–1582, Sept. 1993.
9. T. Colonius, S. K. Lele, and P. Moin. Sound generation in a mixing layer. *J. Fluid Mech.*, 330:375–409, 1997.
10. EAS3 (Ein-Ausgabe-System). http://www.iag.uni-stuttgart.de/eas3.
11. W. Eissler. Numerische Untersuchung zum laminar-turbulenten Strömungsumschlag in Überschallgrenzschichten. *Dissertation, Institut für Aerodynamik und Gasdynamik, Universität Stuttgart*, 1995.
12. J. B. Freund. Noise sources in a low-Reynolds-number turbulent jet at Mach 0.9. *J. Fluid Mech.*, 438:277–305, 2001.
13. M. B. Giles. Nonreflecting boundary conditions for Euler equation calculations. *AIAA J.*, 28(12):2050–2058, 1990.
14. J. Jeong and F. Hussain. On the identification of a vortex. *J. Fluid Mech.*, 285:69–94, 1995.
15. M. J. Kloker. A robust high-resolution split-type compact FD scheme for spatial DNS of boundary-layer transition. *Appl. Sci. Res.*, 59:353–377, 1998.
16. T. J. Poinsot and S. K. Lele. Boundary conditions for direct simulations of compressible viscous flows. *Phys. Fluids*, 101:104–129, 1992.
17. B. Spagnoli. Etude numérique de sensibilité et contrôle optimal du bruit aéroacoustique généré par une couche de mélange compressible bidimensionnelle. *Thèse de doctorat de l'Université Paul Sabatier, Toulouse*, 2006.
18. B. Spagnoli and C. Airiau. Adjoint analysis for noise control in a two-dimensional compressible mixing layer. *Computers and Fluids*, 37(4):475–486, 2008.
19. S. Walther, C. Airiau, and A. Bottaro. Optimal control of Tollmien-Schlichting waves in a developing boundary layer. *Phys. Fluids*, 13:2087–2096, 2001.
20. M. Wei and J. Freund. A noise controlled free shear flow. *J. Fluid Mech.*, 546:123–152, 2006.